Bulk band structure of chromium

P. E. S. Persson and L. I. Johansson
Department of Physics and Measurement Technology, Linköping University, S-581 83 Linköping, Sweden
(Received 22 October 1984; revised manuscript received 7 March 1986)

The bulk band structure of paramagnetic chromium, calculated with use of the linear augmented plane-wave method, is presented and discussed. The calculated band structure is used for interpreting the data obtained in angle-resolved photoemission experiments carried out on Cr(110). Experimentally determined band locations and dispersions are found to agree fairly well with the theoretically predicted values. Calculations of the photocurrent-simulating recorded photoemission spectra have also been made with the use of two different methods, and these results are presented and discussed.

I. INTRODUCTION

The electronic structure of some of the $3d$ transition metals has been the subject of several studies during the last few years.[1–16] The bulk and surface electronic properties have been calculated and checked experimentally. In most cases, electron band-structure calculations based on the one-electron approximation fairly well predict the locations and dispersions of the energy bands. The exception is Ni with, for example, a measured d-band width[9–11] which is about 30% smaller than that theoretically predicted and a satellite structure which appears[17] around 6 eV below the Fermi level. The correlation effects within the unfilled $3d$ bands of Ni seem to explain the discrepancies.[18,19] For the other $3d$ transition metals, however, the treatment of the electronic exchange and correlation effects do not appear to be so critical. Cr is unique among these metals in that an itinerant antiferromagnetic state occurs below the Neél temperature ($T_N = 312$ K for pure Cr). Since the antiferromagnetic state is critically dependent on the electronic band structure of Cr, several band-structure calculations have been initiated. Most of them have been made on the paramagnetic phase, bcc Cr, but a few have also been performed on the antiferromagnetic phase.[1,4–6,20] Only a few experimental investigations of the band structure of Cr have been reported,[14,15] on the other hand, during the last few years. In the present work we aim primarily at studying the bulk band structure of paramagnetic chromium. Efforts were also made to reveal the occurrence of surface states and differences in the electronic structure between the paramagnetic and antiferromagnetic phases of Cr. A self-consistent calculation of the bulk band structure of paramagnetic Cr was made using the linearized augmented plane-wave (LAPW) method.[21] The calculation is based on the one-electron approximation and the local-density approximation for exchange and correlation. The band structure was calculated for energies up to about 25 eV above the Fermi level, thus allowing an interpretation of the results obtained in angle-resolved photoemission measurements made on Cr(110) using the direct-transition model. An experimental mapping of the bulk band structure along the high-symmetry azimuthal directions $\langle 001 \rangle$ and $\langle \bar{1}10 \rangle$ are presented below and compared to the predictions of the band-structure calculation. Photoemission spectra from Cr(110) have also been calculated using two different methods, the time-reversed low-energy electron diffraction (LEED)-theory scheme[22] and a method[23] based on the LAPW band-structure calculation. The latter method models the contribution from bulk (band) emission while the former also includes contributions from surface emission. Calculated photoemission spectra from Cr(110) are presented below and compared with experimental spectra.

II. EXPERIMENTAL

Angle-resolved photoemission experiments were carried out utilizing a Vacuum Generators ADES400 electron spectrometer equipped with a resonance lamp producing unpolarized He I (21.2 eV) and Ne I (16.8 eV) radiation. The electron energy analyzer has an acceptance angle of $\pm 2°$ and was operated at an energy resolution of $\lesssim 0.2$ eV. The base pressure of the instrument is $\lesssim 1 \times 10^{-10}$ torr.

Two Cr(110) samples were utilized in these studies, one pure Cr crystal and one Cr crystal doped with 1.6 at. % Mn. The samples were cut and oriented to within $\pm 1°$ using x-ray diffraction and the surfaces were electropolished in a perchloric and acetic acid mixture prior to mounting. *In situ* cleaning of the samples was performed by sputter-anneal cycles. Ar^+ ions of energies between 0.5–2.5 keV were used for sputtering and annealings were made at temperatures between 600–700 °C. During a few annealings small oxygen exposures were made ($\approx 10^{-7}$ torr of oxygen for a few minutes) in order to get a carbon-free surface. The surface geometry was checked using LEED, and the pattern characteristics of the clean (110) surface were obtained.[24]

Photoemission spectra were recorded at different electron-emission angles, along the two high-symmetry azimuthal directions $\langle 100 \rangle$ and $\langle \bar{1}10 \rangle$. The emission angle θ_e and the incident angle of the radiation θ_i are given relative to the sample surface normal. The Fermi level was used as the reference level in all the spectra presented below. The Cr(110) samples were found to be fairly reac-

tive with the residual gases in the spectrometer, and therefore the sputter-anneal cleaning cycle was repeated about every third hour of data accumulation. The clean Cr(110) surface was also exposed to controlled amounts of pure oxygen in order to reveal surface-related features in the photoemission spectra. A cold finger was attached to the sample holder allowing the sample to be cooled down to below -100 °C, as was measured with a thermocouple spot welded to the side of the sample. Photoemission studies could thus be made at temperatures both well above and below the Néel temperature, which for pure Cr is $T_N = 312$ K.

III. RESULTS AND DISCUSSION

A. Band-structure calculation

One of the most popular schemes for electronic band-structure calculations is based on the density-functional (DF) theory[25] and uses a local approximation for the exchange and correlation potential.[26] Although the eigenvalues resulting from density-functional calculations usually give a good approximation to experimental values, there are some well-known cases where the DF scheme causes substantial deviations, i.e., the d-band width in Ni and the band gap in semiconductors. However, in this calculation no effort was made to include any corrections of the local-density-functional scheme. Instead, one of the purposes was to develop a practical tool for solving a problem often encountered when experimental results are interpreted, namely, that of identifying the contributions of the different possible transitions to a photoemission spectrum.

The linear augmented plane-wave method[21] is widely used for electronic band-structure calculations due to its simple matrix elements and because all the eigenvalues and eigenvectors can be rapidly found. It also gives accurate eigenvalues for both the occupied part of the bands as well as for the higher unoccupied bands. This is important if the calculated bands are to be used for interpreting experimental photoemission results. For this reason we have used the LAPW method to do a self-consistent band-structure calculation of paramagnetic chromium. The calculation was done within the local-density-functional scheme, and we have used the Hedin-Lundqvist approximation[26] for the exchange and correlation potential.

In the LAPW method, the radial wave function is expanded around a chosen energy parameter E_l, and the resulting eigenvalues are most accurate close to this value. An accuracy of a few mRy over an energy range of about 1 Ry can usually be expected.

During the self-consistent iteration we found it convenient to take the E_l values as follows:

$$E_l = \sum_i \varepsilon_i \rho_i(l) \Big/ \sum_i \rho_i(l) ,$$

where ε_i are the eigenvalues of the occupied bands and $\rho_i(l)$ are the integrated partial (l-like) charge density inside the muffin-tin sphere. In Table I we given the final E_l values.

During the self-consistent iteration, both the valence and the core electrons were recalculated. For the core electrons, only the spherical part of the potential was included, while for the valence electrons, non-muffin-tin terms were included in the following way. The potential is divided into two parts, a spherical symmetrical part $V(r)$ valid only inside the muffin-tin spheres and a Fourier sum $\sum_G V_G e^{iG\cdot r}$ valid in the entire cell. The spherical part of the potential and the potential in the interstitial region are included in exact form (the warped muffin-tin potential). The remaining part of the nonspherical potential is included in an approximate way. Since both the amplitude and derivative of the radial wave function are matched to the plane waves at the muffin-tin radius, these plane waves can be used to represent the wave function just inside the muffin-tin radius. Thus the remaining part of the nonspherical potential is included by extending the plane waves inside the spheres.

TABLE I. Final energy parameters E_l for the radial wave functions (in Ry with respect to the Fermi level).

l	E_l
0	−0.34
1	−0.17
2	−0.15
3	−0.12
4	−0.13
5	−0.14
6	−0.14
7	−0.13
8	−0.17

In the band-structure calculation, we have used a basis set of 87 unsymmetrized plane waves. The expansion in spherical harmonics was taken up to $l = 8$. This was found to give a convergence within a few mRy for the occupied part of the bands (some symmetry **k** points were checked with the symmetrized augmented plane-wave method). Our criterion for self-consistency was that the maximum change in the spherical part of the potential should be less than 0.1 mRy. The charge density was constructed from 55 **k** points uniformly distributed on a cubic grid in the irreducible part of the Brillouin zone. In Fig. 1 we show the self-consistent band structure along the symmetry lines. In Table II we compare our results with some earlier calculations. The agreement is seen to be good between this calculation and the linear-combination-of-Gaussian-orbitals calculation done by Laurent *et al.* using the von Barth–Hedin (VBH) potential. They used the same lattice constant $a = 5.4456$ a.u. and performed calculations both for the VBH and the Kohn-Sham-Gaspar (KSG) potential.

The charge density is a ground-state property and can therefore be calculated exactly within the density-functional formalism. This provides an additional possibility to check the accuracy of the approximation used for exchange and correlation by comparing experimental and theoretical x-ray form factors. In Table III we list our values together with the theoretical values obtained by Laurent *et al.* (KSG potential) and some experimental values. There is excellent agreement between the two calculations, and reasonable agreement between theoretical

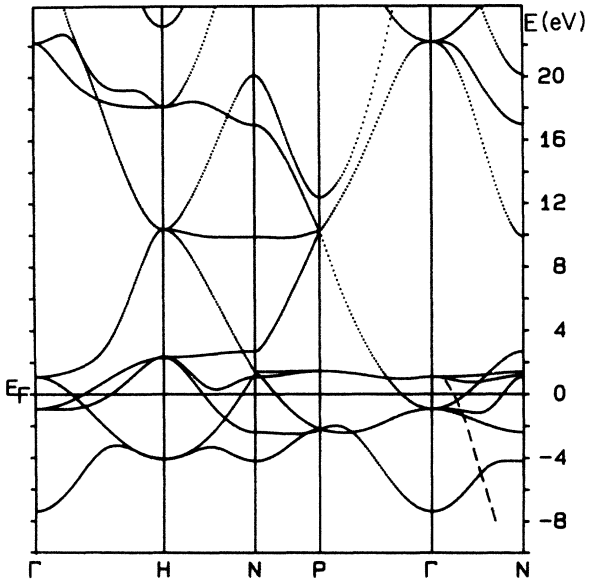

FIG. 1. Self-consistent band structure of paramagnetic chromium, calculated using the LAPW method.

and experimental values, as seen in Table III. To draw any definite conclusions about the charge density from this is difficult, however, because of the fairly large scattering in the experimental data.

B. Photoemission calculation

Symmetry selection rules[27] are often used when trying to interpret spectra since the selection rules usually reduce the number of possible transitions. However, as soon as the symmetry lines are left, it is no longer possible to obtain this extra information. Ambiguities may arise about which transition makes the dominant contribution, and then one needs to compare with calculated results. The time-reversed LEED-theory scheme[22] has proven to be an extremely useful method for calculating photoemission spectra. Results for Cr(110) obtained using this method are presented below. Sometimes, however, it is difficult to identify which initial-state band makes the dominant contribution to a calculated spectrum since this method is based on the one-step model. For band mapping purposes, this is a crucial question and therefore we also tried another method, based on the LAPW program, for calculating photoemission spectra. Briefly, this is the three-step model,[28] where the three steps are optical excitation, transport to the surface, and escape through the surface out into the vacuum. In this calculation, the optical excitation is approximated by vertical transitions and the transition strength is given by the dipole matrix elements.

A compact formula for the three-step model is

$$N(E,\mathbf{K}_{||},\hbar\omega) \propto \sum_{fi} \int d^3k \,|M_{fi}|^2 D(E_f,k) T(E_f,\mathbf{K}_{||}) \times \delta(E_f - E_i - \hbar\omega)\delta(E - E_f) \times \delta(\mathbf{k}_{||} + \mathbf{G}_{||} - \mathbf{K}_{||}) ,$$

where $|M_{fi}|$ stands for the dipole matrix elements, $D(E_f,k)$ simulates the transport to the surface, and $T(E_f,\mathbf{K}_{||})$ is the transmission factor. Lifetime effects were simulated by replacing the two first δ functions with a Lorenzian broadening,

$$\frac{\Gamma(E_f)/2}{(E-E_f)^2+[\Gamma(E_f)/2]^2} \quad \frac{\Gamma(E_i)/2}{(E-E_i-\hbar\omega)^2+[\Gamma(E_i)/2]^2} ,$$

of both the initial and final states. At the surface, the crystal wave function should be matched to the plane-wave solution in the vacuum. In the one-step model the matching at the surface mixes surface states and bulk

TABLE II. Energy differences (in Ry) for paramagnetic chromium.

	Present	Ref. 6 (VBH)	Ref. 6 (KSG)	Ref. 5
$E_F - E_{\Gamma_1}$	0.5420	0.5599	0.5678	0.7143
$E_{\Gamma_{12}} - E_{\Gamma_1}$	0.6220	0.6364	0.6454	0.8210
$E_{\Gamma_{12}} - E_{\Gamma_{25'}}$	0.1471	0.1440	0.1431	0.1715
$E_{\Gamma_{25'}} - E_{\Gamma_1}$	0.4749	0.4924	0.5022	0.6495
$E_{H_{25'}} - E_{H_{12}}$	0.4714	0.4801	0.4877	0.6620
$E_{H_{15}} - E_{\Gamma_1}$	1.3040	1.3201	1.3201	1.3723
$E_{H_{25'}} - E_{\Gamma_{25'}}$	0.2396	0.2387	0.2411	0.3166
$E_{\Gamma_{12}} - E_{H_{12}}$	0.3789	0.3854	0.3897	0.5168
$E_{P_3} - E_{P_4}$	0.2711	0.2719	0.2748	0.3813
$E_{N_2} - E_{N_1}$	0.1336	0.1407	0.1444	0.2089
$E_{N_3} - E_{N_1}$	0.5061	0.5156	0.5235	0.7132
$E_{N_4} - E_{N_{1'}(2)}$	0.0248	0.0228	0.0226	0.0343
$E_{N_{1'}} - E_{N_4}$	−0.0106	−0.0224	−0.0314	−0.1876
$E_{N_3} - E_{N_{1'}}$	0.1052	0.1219	0.1340	0.3303

TABLE III. X-ray form factors for paramagnetic chromium. Present and Ref. 6 are theoretical, Refs. 29, 30, and 31 are experimental values.

Wave vector	Present	Ref. 6	Ref. 33	Ref. 34	Ref. 35
(1,1,0)	16.32	16.29	15.88	15.78±0.20	16.30±0.12
(2,0,0)	13.44	13.39	13.14±0.34	13.13±0.17	
(2,1,1)	11.66	11.66	11.23±0.34	11.47±0.15	
(2,2,0)	10.38	10.39	9.97±0.50	10.20±0.14	
(3,1,0)	9.42	9.40	8.94±0.30		
(2,2,2)	8.79	8.82	8.44±0.16		
(3,2,1)	8.25	8.27	7.75±0.10		
(4,0,0)	7.82	7.76	7.50±0.24		
(4,1,1)	7.50	7.48	7.05±0.09		
(3,3,0)	7.52	7.54	7.05±0.09		
(4,2,0)	7.24	7.23	6.72±0.15		
(3,3,2)	7.02	7.06	6.59±0.19		
(4,2,2)	6.82	6.84	6.41±0.12		

states. However, since the goal was to obtain the pure bulk contribution, a simplified matching was used in this calculation. At the surface, the bulk wave function can be written as a two-dimensional Fourier series over surface reciprocal-lattice vectors. The Bloch state is assumed to be decoupled into such plane waves, and these are then matched to the plane-wave solution in the vacuum, one by one. Thus, the calculation is made in the zero damping limit, and the transmission factor $T(E_f,\mathbf{K}_{||})$ is given by the plane-wave matching. This approximation yields a very simple but still useful expression for the photocurrent, making it possible to get information not only about symmetry selection rules but also about the intensities that can be expected from different transitions, as illustrated below.

C. Band-structure mapping

By using the photoemission technique and the results of the band-structure calculation, we have performed an experimental mapping of the bulk band structure by applying the direct-transition model. At normal electron emission, only Σ_1 final-state bands can contribute to the emission according to symmetry selection rules.[27] The possible direct transitions at a photon energy of 21.2 eV are illustrated in Fig. 1 by the intersections between the initial-state bands and the dashed line which represents the Σ_1 final-state band displaced downwards in energy by 21.2 eV. Four intersections are observed, but since symmetry selection rules state that the Σ_2 initial-state band cannot contribute at normal electron emission, only three remain, two within 1 eV of the Fermi level, E_F, and one about 4.5 eV below E_F.

Photoemission spectra recorded at normal electron emission using He I (21.2 eV) radiation are shown in Fig. 2 for two different incidence angles θ_i. Although the radiation is unpolarized, the relative contribution from Σ_1 and Σ_3 initial-state bands changes when the incidence angle is varied, as seen in Fig. 2. When increasing the incidence angle, the component of the electric field vector parallel to the surface normal increases, which shows up in the spectrum as an increased relative contribution from initial band states of Σ_1 symmetry, in accordance with symmetry selection rules. Thus, structures in the normal emissior spectra originating from the Σ_1 and Σ_3 initial-state bands located close to E_F can be identified unambiguously. However, no structure originating from the lower-lying Σ_1 initial-state band ($\approx$4.5 eV) was observed in these normal emission spectra.

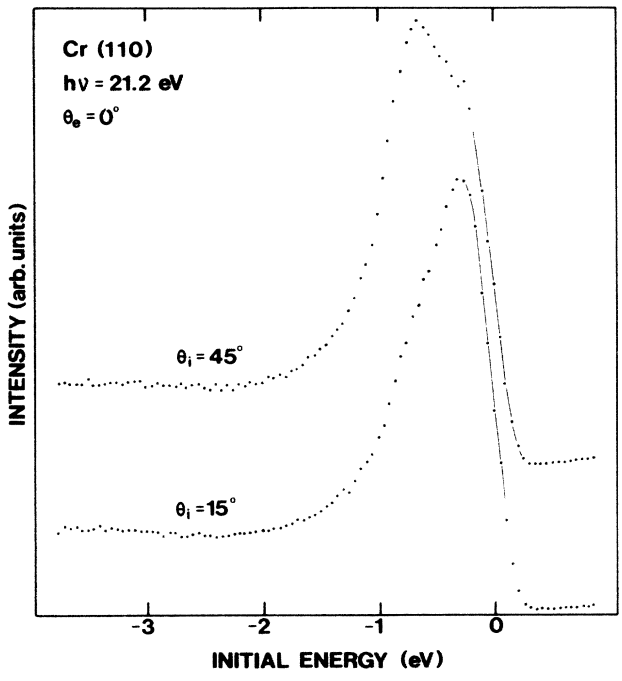

FIG. 2. Angle-resolved photoemission spectra of Cr(110) at normal electron emission ($\theta_e=0°$) and at two different incidence angles, θ_i, in the ⟨001⟩ azimuth, of the unpolarized He I radiation.

An experimental mapping of the bulk band structure was made by varying the electron emission angle θ_e. This was performed in two different azimuthal directions, the $\langle 001 \rangle$ and the $\langle \bar{1}10 \rangle$ directions. Based on the assumption that the momentum component of the photoelectron parallel to the surface can be described as

$$k_{||} = \frac{(2mE_{\text{kin}})^{1/2}}{\hbar} \sin\theta_e ,$$

where m is the free-electron mass and E_{kin} the measured kinetic energy of the emitted electron, theoretical band dispersions were calculated as a function of the electron-emission angle θ_e using the earlier described paramagnetic band-structure results. The experimental and calculated results are summarized in Figs. 3, 4, and 5. The solid lines represent the calculated dispersions and the dots represent experimentally determined locations of the initial-state bands. The vertical bars indicate the estimated uncertainty in the determination of peak positions for cases where it is larger than 0.1 eV. The overall agreement between experimental and calculated results is seen in Figs. 3, 4, and 5 to be fairly good. The major trends in the experimentally determined dispersions are in most cases well reproduced by the calculated dispersions. For example, the structure around -1 eV originating from the Σ_1 initial-state band in the normal emission spectra is seen to disperse downward in energy when the emission angle is increased. Its dispersion with θ_e corresponds fairly closely with the calculated results in all three cases, as seen in Figs. 3, 4, and 5. The predicted splitting of this structure into two or three structures for Ne I radiation at large emission angles (see Figs. 4 and 5) is also observed experimentally. Contribution to the emission from the lower-lying initial-state band around -4 eV is also clearly identified in the off-normal emission spectra in all three cases. However, no structure corresponding to emission from the Σ_2 band at normal emission is observed in the spectra recorded at small emission angles, $\theta_e \leq 10°$.

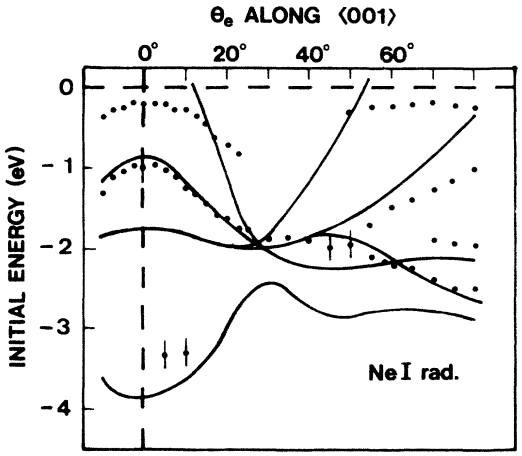

FIG. 4. Comparison between experimental and calculated peak positions as functions of polar angle along the $\langle 001 \rangle$ azimuth for Ne I radiation. See text for details.

There are some branches of the calculated dispersion curves for which no corresponding structures are observed in the recorded spectra. This is most clearly seen in Fig. 3 at emission angles between $30° < \theta_e < 70°$ and for initial-state energies between 0 and -2 eV. It should be noticed that all possible final-state bands were included when the dispersion was calculated. However, the transition probability to some of these bands is actually so small that no corresponding emission is expected to be observed, as will be illustrated by the calculated photoemission spectra shown below.

The band-structure mapping made in the $\langle \bar{1}10 \rangle$ direction using He I radiation is not summarized in a figure. Instead, a few spectra recorded at different emission angles along this azimuth are shown in Fig. 6(a). In this case the two structures observed between 0 and -1 eV in the normal emission spectrum are seen merely to move towards and above the Fermi level, upon increasing the

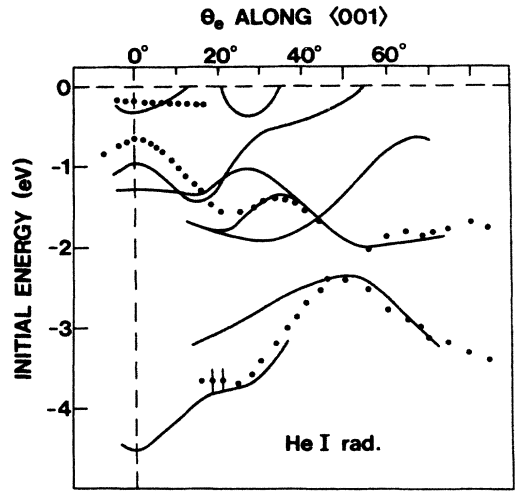

FIG. 3. Comparison between experimental and calculated peak positions as functions of polar angle along the $\langle 001 \rangle$ azimuth for He I radiation. See text for details.

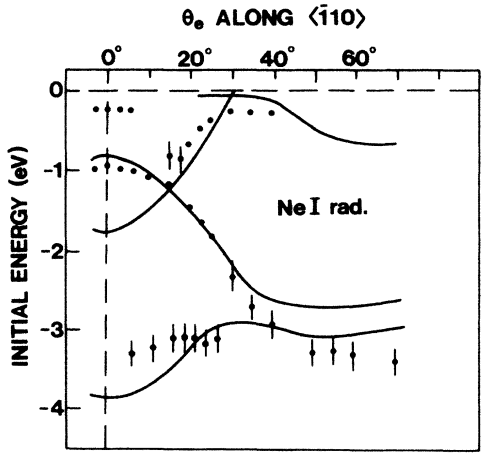

FIG. 5. Comparison between experimental and calculated peak positions as functions of polar angle along the $\langle \bar{1}10 \rangle$ azimuth for Ne I radiation. See text for details.

emission angle. This dispersion, when the emission angle is increased up to about 35°, closely follows the calculated bulk band dispersions. For emission angles larger than about 35°, no sharp prominent structure appears in the experimental spectra between 0 and −4 eV, while several branches appear in the calculated results. These branches originate from final-state bands for which the calculated transition probabilities are so small that no corresponding structures are expected in the recorded spectra. The spectra recorded in this azimuth agree well with the experimental results recently published by another group.[16]

D. Photoemission spectra

In addition to the changes in peak positions, strong modulations of peak intensities are also observed in the photoemission spectrum when the electron-emission angle is varied. This is illustrated in Figs. 6(a), 7(a), 8(a), and 9(a), where spectra recorded at different emission angles using He I and Ne I radiation are shown. We have tried to simulate the modulations of relative peak intensities by performing two different types of calculations of the photocurrent. Photoemission spectra calculated using the time-reversed LEED-theory scheme[22] are presented in Figs. 6(b), 7(b), 8(b), and 9(b). The results obtained using the method based on the LAPW program are presented in Figs. 6(c), 7(c), 8(c), and 9(c). Both types of calculations are based on the self-consistent potential generated for the LAPW band-structure calculation. The broadening parameters introduced which determine the widths of the spectral features were for the low- and high-energy states, 0.0150 and 0.150 Ry, respectively. Since the parameters enter in somewhat different ways into the two types of calculations they do not have to be equal. It should be pointed out that the chosen values are not optimized but instead are merely reasonable values based on experience gained from calculations made on other materials. The calculations were made assuming linearly polarized radiation incident at θ_i along the specified azimuthal direction but with the electric field vector at an angle of 45° relative to the plane of incidence. Although this does not correctly describe the distribution of the electromagnetic field inside the solid we have resorted to this simple distribution in the calculations.

Calculated spectra long the $\langle \bar{1}10 \rangle$ azimuth for He I radiation are presented in Figs. 6(b) and 6(c). At normal emission there are two partly overlapping peaks, one arising from the Σ_3 initial state at about −0.3 eV, and a Σ_1 peak located around −0.9 eV. When the emission angle is increased the two structures disperse up through the Fermi level and disappear at $\theta_e = 40°$. These calculated intensity modulations fairly well reproduce the relative peak intensities in the recorded spectra, shown in Fig. 6(a). A weak structure, located between −3 and −4 eV and arising from the lowest Σ_1 band, is also observed in the calculated spectra, most clearly at off-normal emission. It explains the origin of the weak and broad structure located around −3.5 eV in the experimental spectra.

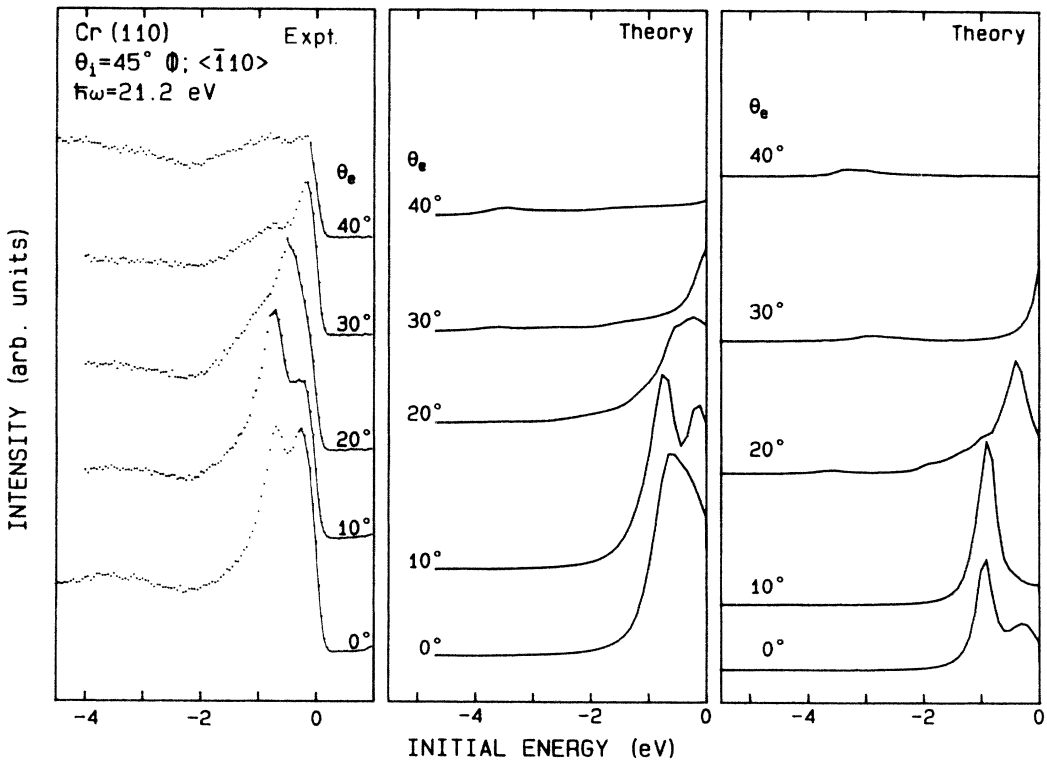

FIG. 6. (a) Angle-resolved He I spectra of Cr(110) recorded at different emission angles in the $\langle \bar{1}10 \rangle$ azimuth and at $\theta_i = 45°$. (b) Theoretical spectra calculated using the time-reversed LEED scheme (Ref. 22), and (c) theoretical spectra calculated using a method (Ref. 23) based on the LAPW program and described in the text.

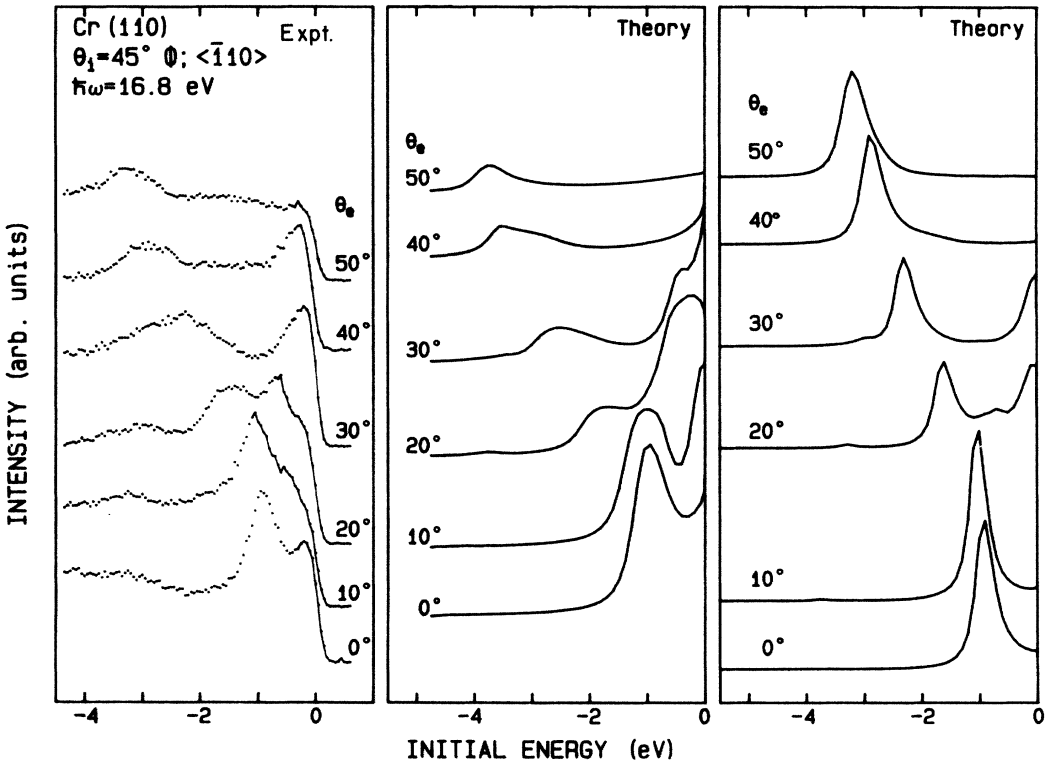

FIG. 7. (a) Angle-resolved Ne I spectra of Cr(110) recorded at different emission angles in the $\langle \bar{1}10 \rangle$ azimuth and at $\theta_i = 45°$. (b) Theoretical spectra calculated using the time-reversed LEED scheme (Ref. 22), and (c) theoretical spectra calculated using a method (Ref. 23) based on the LAPW program and described in the text.

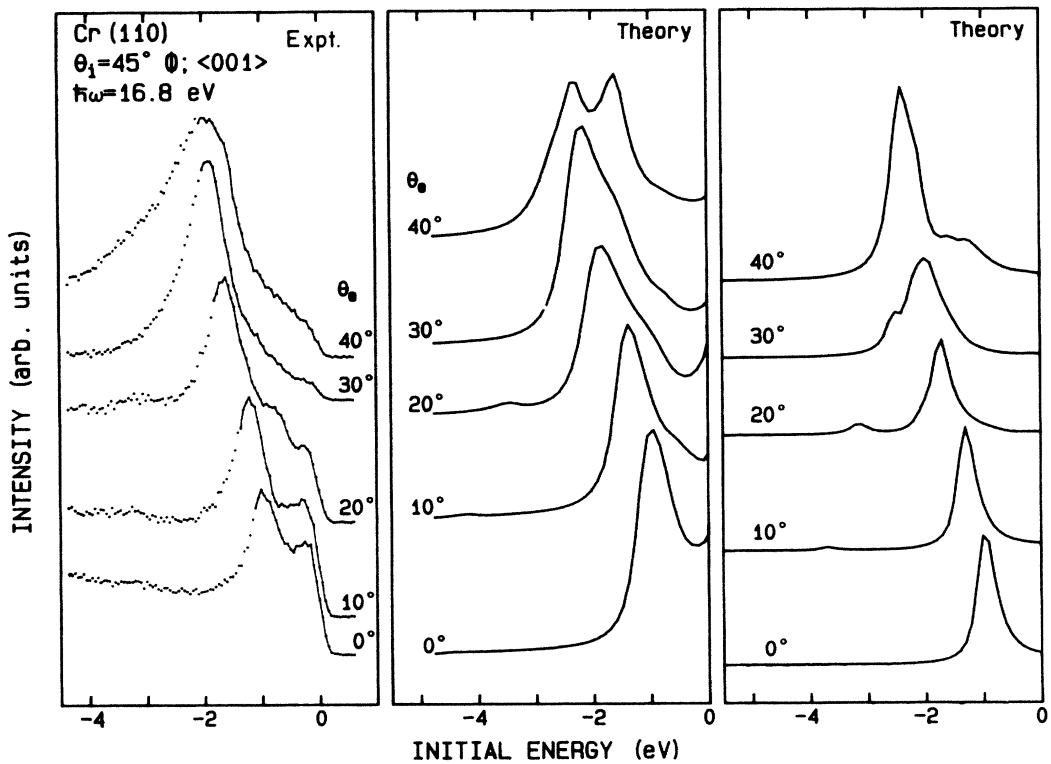

FIG. 8. (a) Angle-resolved Ne I spectra of Cr(110) recorded at different emission angles in the $\langle 001 \rangle$ azimuth and at $\theta_i = 45°$. (b) Theoretical spectra calculated using the time-reversed LEED scheme (Ref. 22), and (c) theoretical spectra calculated using a method (Ref. 23) based on the LAPW program and described in the text.

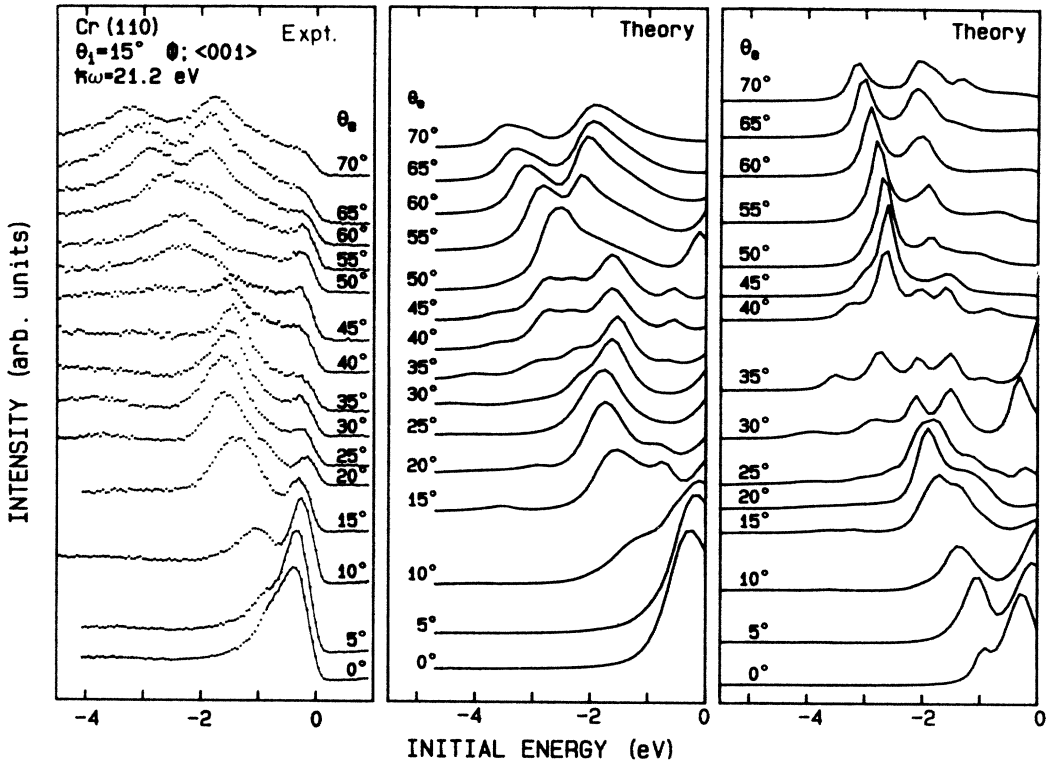

FIG. 9. (a) Angle-resolved He I spectra of Cr(110) recorded at different emission angles in the ⟨001⟩ azimuth and at $\theta_i = 15°$. (b) Theoretical spectra calculated using the time-reversed LEED scheme (Ref. 22), and (c) theoretical spectra calculated using a method (Ref. 23) based on the LAPW program and described in the text.

Calculated results for Ne I radiation along the $\langle \bar{1}10 \rangle$ azimuth are shown in Figs. 7(b) and 7(c). At this energy only the Σ_1 initial-state band contributes to the normal emission spectrum, as shown by the LAPW result in Fig. 7(c). The structure appearing just below the Fermi level at normal emission in the experimental and calculated one-step model spectrum therefore is not interpreted as arising from the Σ_3 initial-state band. Instead, it is interpreted as originating mainly from a surface state.[29] At off-normal emission the Σ_1 peak disperses downwards in energy with increasing emission angle and another peak is seen to be split off at $\theta_e > 10°$ and to disperse up towards the Fermi level. The overall agreement between calculated and experimental spectra is fairly good. The same is true also along the ⟨001⟩ azimuth for Ne I radiation, as shown in Fig. 8. Here the major structure, arising from Σ_1 initial states at normal emission, is seen to disperse downwards in energy with increasing emission angle. Again the near-normal emission LAPW spectra do not show any structure just below the Fermi level, while the experimental and one-step model spectra do, indicating surface-state contribution.

In Fig. 9, the results along the ⟨001⟩ azimuth for He I radiation are presented. At normal emission and an incidence angle of $\theta_i = 15°$ the dominant contribution arises from Σ_3 initial states in both the calculated and experimental spectra. This is expected since symmetry selection rules state that at $\theta_e = 0°$ and the A vector parallel to the surface only Σ_3 initial states can contribute, while only Σ_1 initial states contribute when the A vector is perpendicular to the surface. Emission from the Σ_1 initial-state band appears at off-normal emission and actually gives the major contribution to the spectra at emission angles between about 15° and 40°. The Σ_3 peak disperses up through the Fermi level and disappears around $\theta_e = 15°$. At emission angles above 50° a splitting of the major structure into two peaks is observed in both the theoretical and experimental spectra. The calculated spectra are seen to simulate the recorded spectra surprisingly well. It should be noted that no contribution from the Σ_2 initial-state band has been identified in the spectra. At normal emission, however, the Σ_2 band cannot contribute to the emission for any polarization direction. The calculated emission at small emission angles was found to be so small that it always was drowned by stronger emission from nearby located initial states.

Measurements on the clean Cr(110) surface were also performed at temperatures below the Néel temperature in an attempt to observe changes induced by the magnetic phase transition. For pure Cr the itinerant antiferromagnetism below the Néel temperature is associated with a spin-density wave incommensurate with the crystal lattice. The spin-density wave becomes commensurable[30–32] with the crystal lattice and the Néel temperature increases if Cr is doped with, for example, > 1 at. % Mn.

For this reason, we carried out measurements both on pure and a doped Cr crystal. However, the results were negative in that no significant differences were observed

in the He I and Ne I photoemission spectra recorded at angles close to normal emission at temperatures below and above the Néel temperature. A comparison between calculated photoemission spectra for the paramagnetic and antiferromagnetic phases was also made using Skriver's potentials[4] and the time-reversed LEED-theory scheme. Only very small differences were found in the calculated near-normal emission spectra, when utilizing the broadening parameters applied earlier. Larger differences were observed in the unoccupied part above the Fermi and if the broadening parameters were decreased considerably.

IV. SUMMARY

Using the LAPW method the band structure of paramagnetic Cr was calculated up to energies of about 25 eV above the Fermi level. For the occupied part the results agree very well with earlier published band structures. Our calculated band structure allows a direct interpretation of angle-resolved photoemission experiments performed on Cr(110) using He I and Ne I radiation. By applying the direct transition model a mapping of the bulk band structure was made along two azimuths, the $\langle 001 \rangle$ and $\langle \bar{1}10 \rangle$ directions. A fairly good overall agreement between experimental and calculated band locations and dispersions was obtained. Most of the structures observed in the photoemission spectra could be accounted for by direct bulk transitions. No significant changes were observed in the photoemission spectra recorded close to normal emission at temperatures well above and below the Néel temperature.

Photocurrent calculations were performed using two different methods. How well these calculated results reproduce experimental spectra and observed modulations of peak intensities for different emission angles has been exemplified.

ACKNOWLEDGMENTS

We wish to thank K. F. Berggren for stimulating and helpful discussions, and J. W. Allen for the loan of Cr single crystals. This work was supported in part by the Swedish Natural Science Research Council.

[1]V. L. Moruzzi, J. F. Janak, and A. R. Williams, *Calculated Electronic Properties of Metals* (Pergamon, New York, 1978), and references therein.
[2]D. G. Dempsey, W. R. Grise, and L. Kleinman, Phys. Rev. B **18**, 1270 (1978).
[3]J. L. Erskine, Phys. Rev. Lett. **45**, 1446 (1980).
[4]H. L. Skriver, J. Phys. F **11**, 97 (1981), and references therein.
[5]J. L. Fry, N. E. Brener, J. L. Thompson, and P. H. Dickinson, Phys. Rev. B **29**, 384 (1980).
[6]D. G. Laurent, J. Callaway, J. L. Fry, and N. E. Brener, Phys. Rev. B **23**, 4977 (1981), and references therein.
[7]P. Thiry, D. Chandesris, J. Lecante, C. Guillot, R. Pinchaux, and Y. Petroff, Phys. Rev. Lett. **43**, 82 (1979).
[8]J. A. Knapp, F. J. Himpsel, and D. E. Eastman, Phys. Rev. B **19**, 4952 (1979).
[9]F. J. Himpsel, J. A. Knapp, and D. E. Eastman, Phys. Rev. B **19**, 2919 (1979).
[10]W. Eberhardt and E. W. Plummer, Phys. Rev. B **21**, 3245 (1980).
[11]H. Mårtensson and P. O. Nilsson, Phys. Rev. B 30, 3047 (1984).
[12]D. E. Eastman, F. J. Himpsel, and J. A. Knapp, Phys. Rev. Lett. **44**, 95 (1979).
[13]A. M. Turner and J. L. Erskine, Phys. Rev. B **25**, 1983 (1982).
[14]L. I. Johansson, L. G. Pettersson, K. F. Berggren, and J. W. Allen, Phys. Rev. B **22**, 3294 (1980).
[15]G. Gewinner, J. C. Peruchetti, A. Jaegele, and R. Pinchaux, Phys. Rev. B **27**, 3358 (1983).
[16]P. L. Wincott, N. B. Brookes, D. S. Law, G. Thornton, and H. A. Padmore, Vacuum **33**, 815 (1983).
[17]C. Guillot, Y. Ballu, J. Paigne, J. Lecante, K. P. Jain, P. Thiry, R. Pinchaux, Y. Petroff, and L. M. Falicov, Phys. Rev. Lett. **39**, 1632 (1977).
[18]L. Kleinman and K. Mednick, Phys. Rev. B **24**, 6880 (1981).
[19]S. J. Oh, J. W. Allen, I. Lindau, and J. C. Mikkelsen, Phys. Rev. B **26**, 4845 (1982).
[20]S. Asano and Y. Yamashita, J. Phys. Soc. Jpn. **23**, 714 (1967).
[21]O. K. Andersen, Phys. Rev. B **12**, 3060 (1975).
[22]J. F. L. Hopkinson, J. B. Pendry, and D. J. Titterington, Comput. Phys. Commun. **19**, 69 (1980).
[23]P. E. S. Persson (unpublished).
[24]P. Michel and Ch. Jardin, Surf. Sci. **36**, 478 (1973).
[25]P. Hohenberg and W. Kohn, Phys. Rev. **136**, B864 (1964); W. Kohn and L. J. Sham, *ibid.* **140**, A1133 (1965); R. Gaspar, Acta Phys. Acad. Sci Hung. **3**, 263 (1954).
[26]L. Hedin and B. I. Lundqvist, J. Phys. C **4**, 2064 (1971); U. von Barth and L. Hedin, *ibid.* **5**, 1629 (1972).
[27]J. Hermanson, Solid State Commun. **22**, 9 (1977).
[28]C. N. Berglund and W. E. Spicer, Phys. Rev. **136**, 1030 (1964).
[29]P. E. S. Persson and L. I. Johansson, Phys. Rev. B **33-I**, 8814 (1986).
[30]W. Koehler, R. M. Moon, A. L. Trego, and A. R. Mackintosh, Phys. Rev. **151**, 405 (1966).
[31]C. Stossis, G. R. Kline, and S. R. Sinha, Phys. Rev. Lett. **31**, 1498 (1973); Phys. Rev. B **11**, 2171 (1975).
[32]S. K. Sinha, G. R. Kline, C. Stossis, and N. Chesser, Phys. Rev. B **15**, 1415 (1977).
[33]M. J. Cooper, Philos. Mag. **7**, 2059 (1962); **10**, 177 (1964).
[34]M. Diana and G. Mazzone, Phys. Rev. B **5**, 3832 (1972).
[35]M. Fujimoto, O. Terasaki, and D. Watanabe, Phys. Lett. **41A**, 159 (1972).